Nanometer-Scale Lateral p−n Junctions in Graphene/α-RuCl₃ Heterostructures

Daniel J. Rizzo,□ Sara Shabani,□ Bjarke S. Jessen,□ Jin Zhang,□ Alexander S. McLeod, Carmen Rubio-Verdú, Francesco L. Ruta, Matthew Cothrine, Jiaqiang Yan, David G. Mandrus, Stephen E. Nagler, Angel Rubio,* James C. Hone, Cory R. Dean, Abhay N. Pasupathy,* and D. N. Basov*

ACCESS | Metrics & More | Article Recommendations | SI Supporting Information

ABSTRACT: The ability to create nanometer-scale lateral p−n junctions is essential for the next generation of two-dimensional (2D) devices. Using the charge-transfer heterostructure graphene/α-RuCl₃, we realize nanoscale lateral p−n junctions in the vicinity of graphene nanobubbles. Our multipronged experimental approach incorporates scanning tunneling microscopy (STM) and spectroscopy (STS) and scattering-type scanning near-field optical microscopy (s-SNOM) to simultaneously probe the electronic and optical responses of nanobubble p−n junctions. Our STM/STS results reveal that p−n junctions with a band offset of ∼0.6 eV can be achieved with widths of ∼3 nm, giving rise to electric fields of order 10^8 V/m. Concurrent s-SNOM measurements validate a point-scatterer formalism for modeling the interaction of surface plasmon polaritons (SPPs) with nanobubbles. *Ab initio* density functional theory (DFT) calculations corroborate our experimental data and reveal the dependence of charge transfer on layer separation. Our study provides experimental and conceptual foundations for generating p−n nanojunctions in 2D materials.

KEYWORDS: scanning tunneling microscopy, scanning tunneling spectroscopy, scanning near-field optical microscopy, plasmons, two-dimensional materials, charge transfer
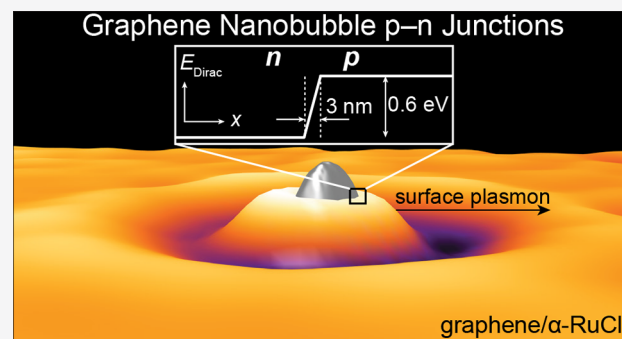
INTRODUCTION

Nanoscale lateral p−n junctions in graphene present promising routes for investigating fundamental quantum phenomena such as Andreev reflection,[1,2] whispering gallery mode resonators,[3,4] quantum dots,[5−9] Veselago lensing,[10,11] and photonic crystals.[12] The ability to realize nanoarchitectures capable of hosting these properties relies on precise control over the lateral p−n junction size, ideally down to atomic length scales. Despite the potential advantages of tailored nanometer junctions, attempts to realize sharp and clean interfacial junctions in graphene-based devices have been limited by the precision of nanolithographic techniques (i.e., >20 nm)[11,13] and lack the nominal potential profile for yielding high-quality devices. Conventional techniques such as local back gating,[13,14] ion implantation,[15,16] and adatoms[17] are practically challenging to implement and can be accompanied by an increase in disorder, reduction in mobility, and surface contamination. Moreover, the maximum charge carrier density achievable with these approaches is typically limited to less than 5×10^{12} cm⁻²,[18,19] restricting the potential gradients accessible with these techniques.

Recent theoretical[20,21] and experimental[22−25] work on graphene/α-RuCl₃ heterostructures demonstrates that the Dirac-point energy (E_{Dirac}) in graphene will experience a massive shift (∼0.6 eV) due to work function-mediated interlayer charge transfer with the underlying α-RuCl₃. While transport measurements suggest a high degree of interlayer charge transfer[23] in graphene/α-RuCl₃ heterostructures (>10^{13} cm⁻²), they have not revealed the lateral dimensions of this charging process. On the other hand, analysis of the plasmonic behavior of graphene/α-RuCl₃ in the vicinity of nanobubbles suggests that boundaries between highly doped and pristine graphene are no wider than 50 nm.[22] Raman maps conducted on these heterostructures produce similar constraints on the maximum size of lateral charge modulation boundaries.[24]
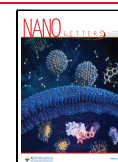
However, a detailed understanding of the nanoscale spatial dependence of interlayer charge transfer between graphene and α-RuCl$_3$ necessitates use of a high-resolution local probe.

In order to elucidate the intrinsic lateral and vertical length scales associated with interlayer charge transfer in graphene/α-RuCl$_3$ heterostructures, we employ two complementary imaging and spectroscopic techniques: scanning tunneling microscopy and spectroscopy (STM/STS) and scattering-type scanning near-field optical microscopy (s-SNOM). STM and STS are ideal probes for studying lateral junction interfaces (e.g., p–n, p–p′, p–i–p, etc.) with atomic resolution and provide information about the local electronic structure (in particular, E_{Dirac} in graphene). On the other hand, s-SNOM uses hybrid light–matter modes known as surface plasmon polaritons (SPPs) to probe the local conductivity in graphene. This multimessenger experimental approach provides a multifaceted view of the fundamental length scales associated with interlayer charge transfer as encoded in both the electronic and plasmonic responses of graphene/α-RuCl$_3$.

We use nanobubbles that arise spontaneously at the graphene/α-RuCl$_3$ heterostructure interface during fabrication as a testbed for probing the in-plane and out-of-plane behavior of interlayer charge transfer. Differential conductivity (dI/dV) maps and point spectroscopy performed at the boundary of nanobubbles reveal that highly p-doped and intrinsically n-doped graphene are separated by a lateral distance of ∼3 nm and vertically by ∼0.5 nm, generating internal fields on the order of 10^8 V/m. In addition, the rapid change in the graphene conductivity in the vicinity of nanobubbles acts as a hard plasmonic barrier that reflects SPPs generated during s-SNOM measurements, as observed previously.[22] The results of STS measurements inform our interpretation of the s-SNOM data and permit us to further develop our model for the complex-valued near-field signal associated with nanobubble-scattered SPPs using a perturbative point-scatterer approach. Our results are well supported by first-principles density functional theory (DFT) calculations, which reveal the origin of the sharp spatial profile of interlayer charge transfer at the boundary of nanobubbles.

RESULTS AND DISCUSSION

The graphene/α-RuCl$_3$ heterostructures studied herein were fabricated using dry transfer techniques from components isolated using exfoliation from single-crystal sources (see Methods and Figure S1 for fabrication process). The resulting heterostructure consists of large regions of graphene forming a flat interface with the underlying α-RuCl$_3$, which are occasionally interrupted by graphene nanobubbles (Figure 1A) (see Figure S2 for STM topographic overview).

A high-magnification topographic STM image of a characteristic graphene nanobubble is shown in Figure 1B. As observed with STM topography, the typical heights of nanobubbles studied in this work were between 1 to 3 nm, while the radius ranged from 20 to 80 nm. Topographic images collected with an atomic force microscope (AFM) used during s-SNOM measurements yield similar nanobubble dimensions (Figure S2). On the other hand, near-field images of these same nanobubbles collected using s-SNOM reveal larger circular features that extend over lateral distances of several hundred nanometers (Figure 1C). The oscillatory nature of the near-field signal moving radially from nanobubbles is consistent with the presence of SPPs that are either being launched or reflected from these locations, giving rise to modulations in the
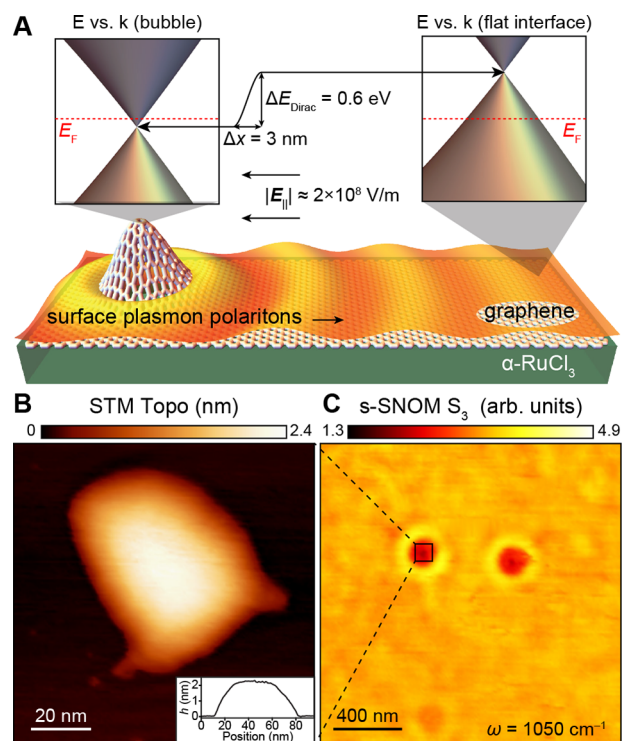

Figure 1. Overview of joint STM/s-SNOM investigation of nanobubbles in graphene/α-RuCl$_3$ heterostructures. (A) Schematic of Dirac-point energy shift between nanobubbles and clean flat interfaces in graphene/α-RuCl$_3$ heterostructures. The ∼0.6 eV energy shift takes place over a lateral length scale of ∼3 nm at the boundary of nanobubbles, generating effective lateral fields of $E_{\parallel} \approx 2 \times 10^8$ V/m (0.2 V/nm). Since the pristine graphene suspended in the nanobubble is intrinsically n-doped, a p–n junction is created at the nanobubble boundary. The associated jump in the graphene conductivity at the perimeter of the nanobubble acts as a hard boundary for reflection of surface plasmon polaritons. (B) Characteristic STM topographic image of a nanobubble (V_S = 0.7 V, I_t = 50 pA). The inset shows the one-dimensional cross section of the nanobubble topography. (C) Characteristic s-SNOM image of two nanobubbles shows circular fringe patterns corresponding to radially propagating surface plasmon polaritons (ω = 1050 cm^{-1}).

near-field signal that extend far beyond the nanobubble area. It has been suggested that these plasmonic features arise due to discontinuities in the graphene conductivity associated with local modulation of charge carrier density,[22] though the precise nature of this profile demands further scrutiny with STM and STS.

In order to gain insight into the spatial dependence of interlayer charge transfer, we performed a series of STM and STS measurements in the vicinity graphene nanobubbles (Figures 2, S3). Figure 2A shows two representative point spectra collected on a flat interface of graphene/α-RuCl$_3$ (red curve) and on a nanobubble (blue curve). The spectrum taken on the nanobubble (blue curve) is characteristic of slightly intrinsically n-doped graphene since E_{Dirac} is located at −100 meV relative to the Fermi energy E_F. This spectrum acts as a reference for the pristine graphene density of states. On the other hand, the dI/dV spectrum on the flat graphene/α-RuCl$_3$ region (red curve) away from the nanobubble junction shows a shift in the Dirac point energy of ΔE_{Dirac} = +625 meV relative to pristine graphene suspended in the nanobubble. This massive shift in E_{Dirac} corresponds to a hole density in graphene
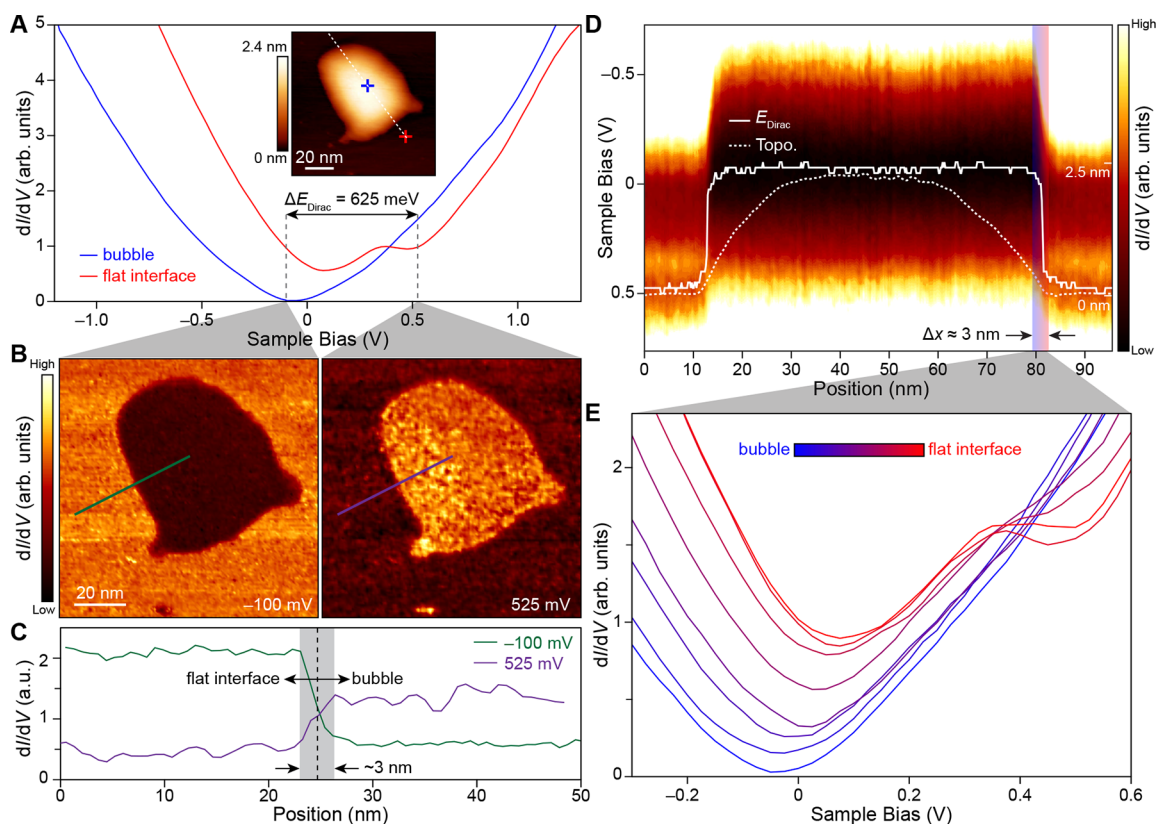
Figure 2. Electronic structure characterization of nanobubbles in graphene/α-RuCl$_3$ using STM and STS. (A) Inset: STM topographic image of a graphene nanobubble (V_S = 0.7 V, I_t = 50 pA). Representative dI/dV point spectroscopy collected over nanobubbles (blue curve) and flat graphene/α-RuCl$_3$ interfaces (red curve) as indicated by the crosshairs in the inset. Between these two spectra, E_{Dirac} shifts by 625 meV. (B) dI/dV maps of a graphene nanobubble conducted at the indicated biases corresponding to the Dirac point energies on the nanobubble (left panel) and the flat interface (right panel) (V_{AC} = 25 mV, I_t = 50 pA). A suppressed LDOS is observed at those biases associated with the local Dirac point energy. (C) Linecuts of the dI/dV maps shown in (B) following the green and purple lines indicated on the −100 and 525 mV maps, respectively. In both instances, the change in the LDOS at the bubble boundary (indicated by the black dashed line) takes place over a lateral length of approximately 3 nm. (D) Position-dependent dI/dV point spectroscopy collected along the dotted white trajectory shown in the inset in (A). The shift in the Dirac point energy occurs over a lateral length scale of ~3 nm as indicated by the region highlighted in partially transparent red and blue. The position-dependence of the Dirac point energy (solid white line) is superimposed on the topographic line cut (dotted white line) showing that the prior has a much more abrupt spatial dependence than the latter. (E) Sample dI/dV point spectra collected at the threshold of a graphene nanobubble corresponding to the red and blue highlighted region in (D).

greater than 10^{13} cm^{-2} resulting from interlayer charge transfer with α-RuCl$_3$. We attribute the local minimum close to E_{F} observed for both spectra to the ubiquitous inelastic tunneling gap that arises due to phonon-mediated processes independent of the graphene doping level.[19] This direct observation of heavily p-doped graphene on α-RuCl$_3$ by STM is consistent with the previous optical and transport studies[22−25] and demonstrates that p−n junctions are formed at the nanobubble boundaries.

To visualize nanobubble p−n junctions, dI/dV maps were conducted at biases corresponding to E_{Dirac} for both the nanobubble and flat interface regions (Figure 2B). The spectroscopic map conducted at −100 mV associated with E_{Dirac} of the nanobubble shows a high LDOS on the surrounding graphene/α-RuCl$_3$ compared to the nanobubble area. A sharp jump in the LDOS is observed at the boundary between these two regions that occurs over a lateral length scale of approximately 3 nm (green curve, Figure 2C). This is consistent with the expectation that the nanobubble should have a suppressed LDOS at its E_{Dirac} compared to the surrounding highly doped regions. By the same reasoning, at +525 mV (i.e., E_{Dirac} of the flat graphene/α-RuCl$_3$ interface)

the LDOS is enhanced on the nanobubble compared to the surrounding flat graphene/α-RuCl$_3$ region. A similarly abrupt shift in the LDOS at the nanobubble edge is observed at this energy (purple curve, Figure 2C). This behavior is characteristic of a nanometer-scale p−n interface in graphene located at the nanobubble boundary. We note that these nanobubble p−n junctions resemble quantum dots previously shown to host quasi-bound states[5−9] that would require a spectral resolution beyond what is achievable in the present room temperature study to be visualized.

We then extracted the potential profile across the p−n junction and evaluated its sharpness. A representative dI/dV line cut is shown in Figure 2D and follows the white trajectory highlighted in the inset of Figure 2A. Figure 2D clearly shows that the local minimum of the Dirac point shifts abruptly at the boundary of the nanobubble from +525 to −100 mV over a length scale of only a few nanometers. To provide information about the correspondence between STM topography and the shift in E_{Dirac}, we compare the nanobubble topographic cross-section (denoted with a white dotted line in Figure 2D) with the position-dependence of E_{Dirac} (solid white line). It is evident that the change in the graphene doping level occurs
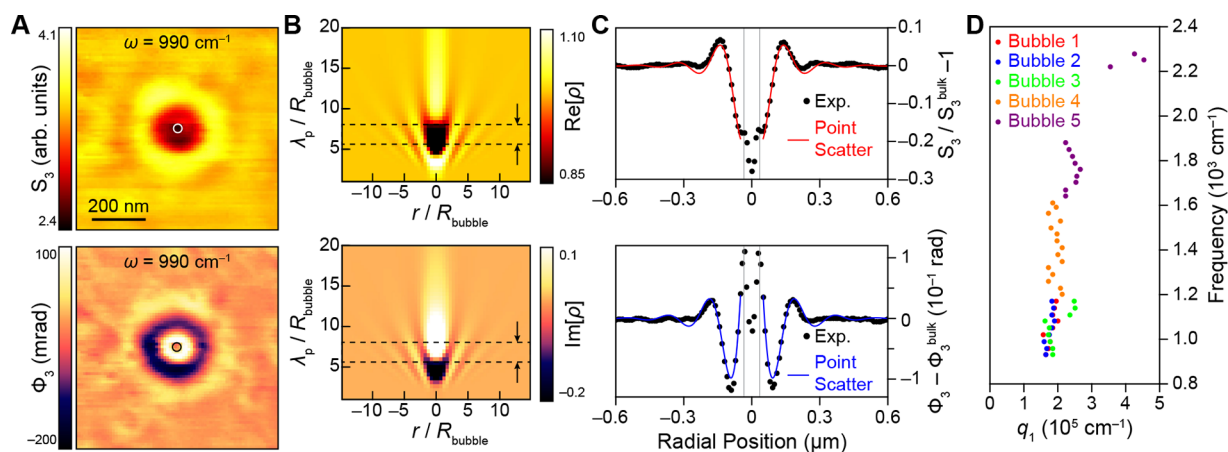
Figure 3. Characterization of the plasmonic response of nanobubbles using s-SNOM. (A) s-SNOM S_3 amplitude (top panel) and Φ_3 phase (bottom panel) collected in the vicinity of a graphene nanobubble ($\omega = 990$ cm^{-1}). The bubble perimeter is indicated in each image with a white and black circle, respectively. A characteristic fringe pattern is observed in both the near-field amplitude and phase emanating radially from the bubble. (B) Simulated near-field amplitude (top panel) and phase (bottom panel) based on a raster-scanned dipole over a conductivity defect with fixed radius R_{bubble} and a variable SPP wavelength λ_p. The radial dependence r/R_{bubble} of both amplitude and phase are shown. The black arrows and black dashed box enclose the regime of λ_p/R_{bubble} that resembles the experimental data. (C) Radial line cuts of the images shown in (A) averaged over half annuli with thicknesses of $\Delta r = 10$ nm. The gray vertical lines indicate the boundaries of the nanobubble. On the basis of a model that treats the nanobubble as a point scatterer, the radial dependence of the experimental near-field amplitude and phase is simultaneously fit to the real and imaginary components of $-A[H_1^{(1)}(q_p r)]^2$, respectively ($H_1^{(1)}$ is the Hankel function of first kind of order one, q_p is the complex SPP wavevector, r is the radial coordinate, and A is a complex amplitude). (D) The corresponding dispersion of SPPs emanating from five different nanobubbles is extracted using the fitting procedure described in (C).

much more abruptly than the height profile of the nanobubble, implying that interlayer charge transfer is rapidly suppressed with interlayer separation. The lateral junction width is measured to be ~3 nm as indicated in Figure 2D. The lateral width of this depletion region is roughly 1 order of magnitude smaller than previously reported results on state-of-the-art split back gate devices.[13] To provide a step-by-step view of the evolution of E_{Dirac} across the junction, a few spectra from the junction region are shown in Figure 2E. Once the interface of the nanobubble is reached and the graphene is separated from the underlying α-RuCl$_3$ layer by less that 1 Å, the minimum corresponding to the Dirac point at +525 mV rapidly shifts to lower biases. Beyond this point, E_{Dirac} shifts more gradually until it reaches its minimum value of −100 mV. (The dependence of the shift in E_{Dirac} on the nanobubble height is shown explicitly in Figure 4D.)

Armed with the results of STM and STS experiments, we now return to s-SNOM images conducted on graphene nanobubbles. Data were collected on five different nanobubbles over a frequency range of 930−2280 cm^{-1} (Figure 3). Characteristic images of the near-field amplitude and phase for $\omega = 990$ cm^{-1} are shown in Figure 3A. Immediately outside the radius of the nanobubble, radial oscillations of both near-field channels decay as a function of distance as shown in Figure 3C. As expected,[22] the spacing between fringes clearly disperses with frequency (Figure S4). In principle, these fringes could arise from SPPs generated on and propagating away from nanobubbles (λ_p fringes), from SPPs generated at the AFM tip that reflect from the nanobubble boundary ($\lambda_p/2$ fringes), or from both. Previous work on similar heterostructures would suggest the near-field behavior is primarily dominated by the latter.[22]

To definitively resolve this question, it is useful to consider that the STS data provides unambiguous evidence that the entirety of the graphene nanobubble consists of nominally undoped graphene surrounded by highly doped graphene with

a boundary width on the order of only a few nanometers. We therefore model the s-SNOM data of a graphene nanobubble as a raster-scanned dipole over a circular conductivity depletion region surrounded by a bulk possessing high conductivity in a manner similar to our previous study[22] (Figure 3B, see Supporting Information for model description). Expanding on this previous work, we now consider that the SPPs generated at the AFM tip during s-SNOM measurements may possess a wide range of wavelengths relative to the size of the nanobubble. At one extreme, the SPP wavelength is much larger than the nanobubble and can pass through with little to no scattering. Here, a maximum in both the near-field amplitude and phase is observed at the location immediately outside the nanobubble boundary. At the other extreme, the SPP wavelength is too small to effectively couple to a finite-sized tip, suppressing the generation of SPPs. At intermediate length scales where the SPP wavelength is on the order of several times the nanobubble dimensions, plasmonic reflections are observed that result in $\lambda_p/2$ fringes whose amplitude scale as $\left(\dfrac{R_{bubble}}{\lambda_p}\right)^2$ (R_{bubble} is the nanobubble radius) (Figure 3B). In contrast to the behavior at large λ_p, here the near-field amplitude possesses a minimum immediately outside the defect, while the phase has a maximum. A comparison of the experimental and simulated near-field images shown in Figure 3A,B suggests that our experiment takes place in this intermediate regime where plasmonic reflections give rise to $\lambda_p/2$ fringes that generate an amplitude minimum and phase maximum at the nanobubble boundary (indicated by the black dashed boxed region in Figure 3B). In principle, λ_p fringes could exist concurrently as a result of light scattering directly from vacuum into the graphene from the nanobubble itself. Such fringes would have a systematic angular-dependent near-field signal enforced by the angle of the incident light projected onto the 2D plane. Since a systematic angular dependence is neither observed in near-field amplitude nor phase (Figure S4),

we exclude the possibility that λ_p fringes are substantially contributing to the observed SPP oscillations.

An approximate representation of the radial dependence of the near-field amplitude can be derived by perturbatively treating the nanobubble as a point scatterer. This is a 2D analogue of Rayleigh scattering and may be useful for analysis of SPP dispersions in a manner analogous to quasiparticle interference (QPI) of 2D electronic states.[26,27] Within this framework, the scattered polariton field is used as a proxy for the near-field signal and has the functional form of $-A[H_1^{(1)}(q_p r)]^2$, (here, $H_1^{(1)}$ is the Hankel function of the first kind of order one, $q_p = q_1 + iq_2$ is the complex SPP wavevector, r is the radial coordinate, and A is a complex scaling factor) (see Supporting Information for full derivation). The real and imaginary components of this function are simultaneously fit to the near-field amplitude and phase, respectively, using A and q_p as fitting parameters. The resulting model line profiles faithfully reproduce the experimental data (Figure 3C). Repeating this fitting procedure for all experimental frequencies ω and all five bubbles yields the SPP dispersion $\omega(q_1)$ (Figure 3D). The shape of the experimental dispersion is consistent with SPPs propagating in highly doped graphene.

Both experimental STM/STS and s-SNOM data provide corroborating evidence that interlayer charge transfer between graphene and α-RuCl$_3$ is eliminated in nanobubbles as a result of <1 nm of interlayer separation. We now inquire into the precise mechanism by which this charge transfer takes place and how it is suppressed in nanobubbles through a series of DFT calculations on model graphene/α-RuCl$_3$ heterostructures. Specifically, we explored the role of an intermediate vacuum region between the two layers varying from 0 to 5 Å above the equilibrium separation (Figure 4A). As reported previously,[22] the shift in E_{Dirac} for the graphene/α-RuCl$_3$ heterostructure with an equilibrium interlayer separation ($h_{min} = 3.3$ Å) is observed to be 0.54 eV (Figure 4B), which is in good agreement with the experimental data on flat interface regions. Expanding on this previous result, we show that the theoretical shift in E_{Dirac} effectively disappears once a vacuum spacer layer of just $\Delta h = h - h_{min} = 5$ Å is introduced (Figure 4C), revealing a rapid decay in the interlayer charge transfer with layer separation. The theoretical dependence of ΔE_{Dirac} at intermediate interlayer separations shows a rapid jump for $\Delta h < 1$ Å followed by a more gradual decay in the interlayer charge transfer at larger separations (Figure 4D). The experimental counterpart to this data can be extracted from Figure 2D to visualize ΔE_{Dirac} as a function of the interlayer separation between graphene and α-RuCl$_3$. Here, ΔE_{Dirac} is obtained from the local minima (or curvature maxima when E_{Dirac} presents as a shoulder) of each dI/dV spectrum taken at a known height above the flat region. Figure 4D demonstrates that the behavior of the model DFT calculation mirrors the experimental STS: both show two characteristic decay lengths of less than and on the order of a few angstroms, respectively. We speculate that the emergence of two characteristic length scales associated with interlayer charge transfer arises due to a dual mechanism involving short-range interlayer tunneling and long-range electrostatic effects between the layers.

The agreement between theory and experiment shows that the magnitude of interlayer charge transfer is agnostic to the surrounding in-plane charge and strain[28] environment (i.e., purely dependent on the layer separation). Thus, it would
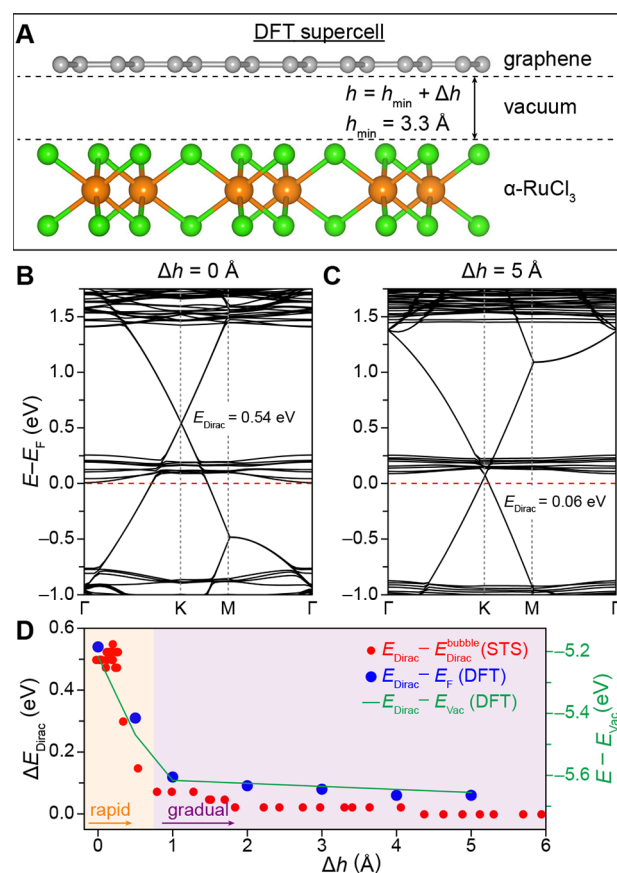

Figure 4. DFT and STM analysis of interlayer charge transfer in graphene/α-RuCl$_3$ heterostructures. (A) Side-view of the graphene/α-RuCl$_3$ heterostructure supercell used in DFT calculations. An equilibrium interlayer separation of $h_{min} = 3.3$ Å is used to model the so-called flat interface observed experimentally. To model the charge transfer behavior between graphene and α-RuCl$_3$ at the edge of nanobubbles (where the interlayer separation increases gradually), additional calculations are performed using interlayer separations of $\Delta h = h - h_{min} = 0.5$, 1, 2, 3, 4, and 5 Å. Orange, green, and gray spheres indicate Ru, Cl, and C atoms, respectively. (B) DFT-calculated band structure for a graphene/α-RuCl$_3$ heterostructure with maximal charge transfer (i.e., $h = h_{min} = 3.3$ Å). (C) Band structure for graphene/α-RuCl$_3$ heterostructure with $h = h_{min} + 5$ Å, showing minimal interlayer charge transfer. The Fermi levels are set to zero in (B,C). (D) The shift in E_{Dirac} relative to its value on the nanobubble plotted as a function of interlayer separation is plotted for both experimental (red dots) and theoretical (blue dots) data. The shift in E_{Dirac} relative to the vacuum energy E_{Vac} is plotted with a green curve. The rapid decay in interlayer charge transfer is highlighted in orange, while the subsequent gradual decay is highlighted in purple.

appear that there is little to no charge redistribution in the graphene plane across the nanobubble interface despite large differences in the local charge carrier density. To understand this, we return to the DFT calculations of model heterostructures with variable vacuum spacer layers and plot ΔE_{Dirac} relative to the vacuum energy (green curve in Figure 4D). From this, it is clear that an electrostatic barrier comparable to the offset in E_{Dirac} of ∼0.6 eV emerges between the pristine nanobubble and the highly doped graphene/α-RuCl$_3$ region. Ultimately, this large electrostatic barrier enforces the sharp p–n junctions naturally generated in nanobubbles.

Finally, we consider the influence of screening on p–n nanojunctions. Poor screening in graphene permits long-range

inhomogeneous potentials extending >100 nm from metallic contacts.[29,30] Contrary to this behavior, mutual doping at the graphene/α-RuCl$_3$ interface leads to the formation of an interlayer dipole that is largely confined to the first atomic layers of the heterojunction interface.[22] The electrostatics of this situation are analogous to a split gate device, where the lateral length scale of the associated bare potential near p−n junctions scales with the thickness of the gate dielectric (can be substantially smaller than 100 nm[13]). In this context, the poor screening in graphene is less relevant to the resulting minimum feature size than the length scale of the underlying bare potential. For graphene/α-RuCl$_3$, the effective gate dielectric thickness is on the order of the layer separation (<1 nm), permitting nanometer-scale depletion regions at nanobubble boundaries.

CONCLUSION

We have measured the electronic and photonic behavior of nanobubbles in graphene/α-RuCl$_3$ heterostructures, revealing massive shifts in the local interlayer charge transfer over lateral length scales of only a few nanometers. Such narrow p−n junctions in graphene have previously been inaccessible using standard doping techniques and have many potential applications for studying fundamental electronic structure properties in graphene and related materials. At the same time, our results demonstrate that work function mediated charge transfer is a viable route toward creating nanoscale conductivity features in graphene that act as local plasmon scatterers. The insights gained in our DFT calculations provide a detailed understanding of the dependence of charge transfer on interlayer separation and reveal abrupt electrostatic barriers at nanobubble boundaries that give rise to nanometer p−n junctions. This work provides the experimental and conceptual foundation for future device design, and validates the use of interstitial layers in charge-transfer heterostructures to predictively influence the local electronic and plasmonic behavior.

METHODS

Experimental and theoretical methods can be found in the Supporting Information.

ASSOCIATED CONTENT

Ⓢ Supporting Information

The Supporting Information is available free of charge at https://pubs.acs.org/doi/10.1021/acs.nanolett.1c04579.

> Additional details about sample fabrication, STM and AFM topography, auxiliary STS and s-SNOM data, experimental and theoretical methods, and derivations for models of the near-field data (PDF)

AUTHOR INFORMATION

Corresponding Authors

D. N. Basov − *Department of Physics, Columbia University, New York, New York 10027, United States;* Email: db3056@columbia.edu

Abhay N. Pasupathy − *Department of Physics, Columbia University, New York, New York 10027, United States; Condensed Matter Physics and Materials Science Department, Brookhaven National Laboratory, Upton, New York 11973, United States;* ⓞ orcid.org/0000-0002-2744-0634; Email: apn2108@columbia.edu

Angel Rubio − *Theory Department, Max Planck Institute for Structure and Dynamics of Matter and Center for Free-Electron Laser Science, 22761 Hamburg, Germany; Center for Computational Quantum Physics, Flatiron Institute, New York, New York 10010, United States; Nano-Bio Spectroscopy Group, Universidad del País Vasco UPV/EHU, San Sebastián 20018, Spain;* ⓞ orcid.org/0000-0003-2060-3151; Email: angel.rubio@mpsd.mpg.de

Authors

Daniel J. Rizzo − *Department of Physics, Columbia University, New York, New York 10027, United States;* ⓞ orcid.org/0000-0003-4587-4863

Sara Shabani − *Department of Physics, Columbia University, New York, New York 10027, United States*

Bjarke S. Jessen − *Department of Physics and Department of Mechanical Engineering, Columbia University, New York, New York 10027, United States;* ⓞ orcid.org/0000-0001-8453-6125

Jin Zhang − *Theory Department, Max Planck Institute for Structure and Dynamics of Matter and Center for Free-Electron Laser Science, 22761 Hamburg, Germany;* ⓞ orcid.org/0000-0001-7830-3464

Alexander S. McLeod − *Department of Physics, Columbia University, New York, New York 10027, United States; Present Address: School of Physics and Astronomy, University of Minnesota, Minneapolis, MN 55455*

Carmen Rubio-Verdú − *Department of Physics, Columbia University, New York, New York 10027, United States*

Francesco L. Ruta − *Department of Physics and Department of Applied Physics and Applied Mathematics, Columbia University, New York, New York 10027, United States*

Matthew Cothrine − *Department of Materials Science and Engineering, University of Tennessee, Knoxville, Tennessee 37996, United States*

Jiaqiang Yan − *Department of Materials Science and Engineering, University of Tennessee, Knoxville, Tennessee 37996, United States; Materials Science and Technology Division, Oak Ridge National Laboratory, Oak Ridge, Tennessee 37831, United States*

David G. Mandrus − *Department of Materials Science and Engineering, University of Tennessee, Knoxville, Tennessee 37996, United States; Materials Science and Technology Division, Oak Ridge National Laboratory, Oak Ridge, Tennessee 37831, United States;* ⓞ orcid.org/0000-0003-3616-7104

Stephen E. Nagler − *Neutron Scattering Division, Oak Ridge National Laboratory, Oak Ridge, Tennessee 37831, United States*

James C. Hone − *Department of Mechanical Engineering, Columbia University, New York, New York 10027, United States*

Cory R. Dean − *Department of Physics, Columbia University, New York, New York 10027, United States*

Complete contact information is available at:
https://pubs.acs.org/10.1021/acs.nanolett.1c04579

Author Contributions

▢D.J.R., S.S., B.S.J. and J.Z. contributed equally. S.S. performed the STM/STS measurements. S.S., C.R.-V., and D.J.R. conducted the STS analysis. A.N.P. advised STM/STS measurements. D.J.R. performed all s-SNOM measurements and analysis. D.N.B. advised s-SNOM measurements. A.S.M.

REFERENCES

(1) Beenakker, C. W. J. Specular Andreev Reflection in Graphene. *Phys. Rev. Lett.* **2006**, *97*, 067007.

(2) Ossipov, A.; Titov, M.; Beenakker, C. W. J. Reentrance Effect in a Graphene N-P-N Junction Coupled to a Superconductor. *Phys. Rev. B* **2007**, *75*, 241401.

(3) Zhao, Y.; Wyrick, J.; Natterer, F. D.; Rodriguez-Nieva, J. F.; Lewandowski, C.; Watanabe, K.; Taniguchi, T.; Levitov, L. S.; Zhitenev, N. B.; Stroscio, J. A. Creating and Probing Electron Whispering-Gallery Modes in Graphene. *Science* **2015**, *348*, 672.

(4) Le, T. L.; Nguyen, V. L. Quantitative Study of Electronic Whispering Gallery Modes in Electrostatic-Potential Induced Circular Graphene Junctions. *J. Phys.: Condens. Matter* **2020**, *32*, 255502.

(5) Lee, J.; Wong, D.; Velasco, J., Jr.; Rodriguez-Nieva, J. F.; Kahn, S.; Tsai, H.-Z.; Taniguchi, T.; Watanabe, K.; Zettl, A.; Wang, F.; Levitov, L. S.; Crommie, M. F. Imaging Electrostatically Confined Dirac Fermions in Graphene Quantum Dots. *Nat. Phys.* **2016**, *12*, 1032−1036.

(6) Gutiérrez, C.; Brown, L.; Kim, C.-J.; Park, J.; Pasupathy, A. N. Klein Tunnelling and Electron Trapping in Nanometre-Scale Graphene Quantum Dots. *Nat. Phys.* **2016**, *12*, 1069−1075.

(7) Gutiérrez, C.; Walkup, D.; Ghahari, F.; Lewandowski, C.; Rodriguez-Nieva, J. F.; Watanabe, K.; Taniguchi, T.; Levitov, L. S.; Zhitenev, N. B.; Stroscio, J. A. Interaction-Driven Quantum Hall Wedding Cake−Like Structures in Graphene Quantum Dots. *Science* **2018**, *361*, 789.

(8) Velasco, J.; Lee, J.; Wong, D.; Kahn, S.; Tsai, H.-Z.; Costello, J.; Umeda, T.; Taniguchi, T.; Watanabe, K.; Zettl, A.; Wang, F.; Crommie, M. F. Visualization and Control of Single-Electron Charging in Bilayer Graphene Quantum Dots. *Nano Lett.* **2018**, *18*, 5104−5110.

(9) Pereira, J. M.; Mlinar, V.; Peeters, F. M.; Vasilopoulos, P. Confined States and Direction-Dependent Transmission in Graphene Quantum Wells. *Phys. Rev. B* **2006**, *74*, 045424.

(10) Cheianov, V. V.; Fal'ko, V.; Altshuler, B. L. The Focusing of Electron Flow and a Veselago Lens in Graphene p-n Junctions. *Science* **2007**, *315*, 1252.

(11) Lee, G.-H.; Park, G.-H.; Lee, H.-J. Observation of Negative Refraction of Dirac Fermions in Graphene. *Nat. Phys.* **2015**, *11*, 925−929.

(12) Xiong, L.; Forsythe, C.; Jung, M.; McLeod, A. S.; Sunku, S. S.; Shao, Y. M.; Ni, G. X.; Sternbach, A. J.; Liu, S.; Edgar, J. H.; Mele, E. J.; Fogler, M. M.; Shvets, G.; Dean, C. R.; Basov, D. N. Photonic Crystal for Graphene Plasmons. *Nat. Commun.* **2019**, *10*, 4780.

(13) Zhou, X.; Kerelsky, A.; Elahi, M. M.; Wang, D.; Habib, K. M. M.; Sajjad, R. N.; Agnihotri, P.; Lee, J. U.; Ghosh, A. W.; Ross, F. M.; Pasupathy, A. N. Atomic-Scale Characterization of Graphene P−N Junctions for Electron-Optical Applications. *ACS Nano* **2019**, *13*, 2558−2566.

(14) Özyilmaz, B.; Jarillo-Herrero, P.; Efetov, D.; Kim, P. Electronic Transport in Locally Gated Graphene Nanoconstrictions. *Appl. Phys. Lett.* **2007**, *91*, 192107.

(15) Willke, P.; Amani, J. A.; Sinterhauf, A.; Thakur, S.; Kotzott, T.; Druga, T.; Weikert, S.; Maiti, K.; Hofsäss, H.; Wenderoth, M. Doping of Graphene by Low-Energy Ion Beam Implantation: Structural, Electronic, and Transport Properties. *Nano Lett.* **2015**, *15*, 5110−5115.

(16) Wang, G.; Zhang, M.; Chen, D.; Guo, Q.; Feng, X.; Niu, T.; Liu, X.; Li, A.; Lai, J.; Sun, D.; Liao, Z.; Wang, Y.; Chu, P. K.; Ding, G.; Xie, X.; Di, Z.; Wang, X. Seamless Lateral Graphene P-N Junctions Formed by Selective in Situ Doping for High-Performance Photodetectors. *Nat. Commun.* **2018**, *9*, 5168−5168.

(17) Praveen, C.; Piccinin, S.; Fabris, S. Adsorption of Alkali Adatoms on Graphene Supported by the Au/Ni (111) Surface. *Phys. Rev. B* **2015**, *92*, 075403.

(18) Dean, C. R.; Young, A. F.; Meric, I.; Lee, C.; Wang, L.; Sorgenfrei, S.; Watanabe, K.; Taniguchi, T.; Kim, P.; Shepard, K. L.; Hone, J. Boron Nitride Substrates for High-Quality Graphene Electronics. *Nat. Nanotechnol.* **2010**, *5*, 722−726.

(19) Zhang, Y.; Brar, V. W.; Wang, F.; Girit, C.; Yayon, Y.; Panlasigui, M.; Zettl, A.; Crommie, M. F. Giant Phonon-Induced Conductance in Scanning Tunnelling Spectroscopy of Gate-Tunable Graphene. *Nat. Phys.* **2008**, *4*, 627−630.

(20) Biswas, S.; Li, Y.; Winter, S. M.; Knolle, J.; Valentí, R. Electronic Properties of A-Rucl$_3$ in Proximity to Graphene. *Phys. Rev. Lett.* **2019**, *123*, 237201.

(21) Gerber, E.; Yao, Y.; Arias, T. A.; Kim, E.-A. Ab Initio Mismatched Interface Theory of Graphene on A-Rucl$_3$: Doping and Magnetism. *Phys. Rev. Lett.* **2020**, *124*, 106804.

(22) Rizzo, D. J.; Jessen, B. S.; Sun, Z.; Ruta, F. L.; Zhang, J.; Yan, J.-Q.; Xian, L.; McLeod, A. S.; Berkowitz, M. E.; Watanabe, K.; Taniguchi, T.; Nagler, S. E.; Mandrus, D. G.; Rubio, A.; Fogler, M. M.; Millis, A. J.; Hone, J. C.; Dean, C. R.; Basov, D. N. Charge-Transfer Plasmon Polaritons at Graphene/A-Rucl$_3$ Interfaces. *Nano Lett.* **2020**, *20*, 8438−8445.

(23) Zhou, B.; Balgley, J.; Lampen-Kelley, P.; Yan, J. Q.; Mandrus, D. G.; Henriksen, E. A. Evidence for Charge Transfer and Proximate Magnetism in Graphene-A-Rucl$_3$ Heterostructures. *Phys. Rev. B* **2019**, *100*, 165426.

(24) Wang, Y.; Balgley, J.; Gerber, E.; Gray, M.; Kumar, N.; Lu, X.; Yan, J.-Q.; Fereidouni, A.; Basnet, R.; Yun, S. J.; Suri, D.; Kitadai, H.; Taniguchi, T.; Watanabe, K.; Ling, X.; Moodera, J.; Lee, Y. H.; Churchill, H. O. H.; Hu, J.; Yang, L.; Kim, E.-A.; Mandrus, D. G.; Henriksen, E. A.; Burch, K. S. Modulation Doping Via a Two-Dimensional Atomic Crystalline Acceptor. *Nano Lett.* **2020**, *20*, 8446−8452.

(25) Mashhadi, S.; Kim, Y.; Kim, J.; Weber, D.; Taniguchi, T.; Watanabe, K.; Park, N.; Lotsch, B.; Smet, J. H.; Burghard, M.; Kern, K. Spin-Split Band Hybridization in Graphene Proximitized with A-Rucl3 Nanosheets. *Nano Lett.* **2019**, *19*, 4659−4665.

(26) Crommie, M. F.; Lutz, C. P.; Eigler, D. M. Imaging Standing Waves in a Two-Dimensional Electron Gas. *Nature* **1993**, *363*, 524−527.

(27) Roushan, P.; Seo, J.; Parker, C. V.; Hor, Y. S.; Hsieh, D.; Qian, D.; Richardella, A.; Hasan, M. Z.; Cava, R. J.; Yazdani, A. Topological Surface States Protected from Backscattering by Chiral Spin Texture. *Nature* **2009**, *460*, 1106−1109.
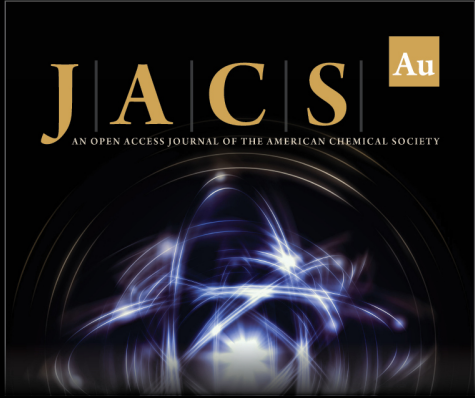
(28) Levy, N.; Burke, S. A.; Meaker, K. L.; Panlasigui, M.; Zettl, A.; Guinea, F.; Neto, A. H. C.; Crommie, M. F. Strain-Induced Pseudo−Magnetic Fields Greater Than 300 T in Graphene Nanobubbles. *Science* **2010**, *329*, 544−547.

(29) Khomyakov, P. A.; Starikov, A. A.; Brocks, G.; Kelly, P. J. Nonlinear Screening of Charges Induced in Graphene by Metal Contacts. *Phys. Rev. B* **2010**, *82*, 115437.

(30) Mueller, T.; Xia, F.; Freitag, M.; Tsang, J.; Avouris, P. Role of Contacts in Graphene Transistors: A Scanning Photocurrent Study. *Phys. Rev. B* **2009**, *79*, 245430.

■ NOTE ADDED AFTER ASAP PUBLICATION

This paper was published ASAP on February 28, 2022, with an error in the Figure 1 caption. The corrected version was reposted on March 9, 2022.